UNIVERSITY OF LEEDS

This is a repository copy of *Role of Structure and Defect Chemistry in High-Performance Thermoelectric Bismuth Strontium Cobalt Oxides*.

White Rose Research Online URL for this paper:
http://eprints.whiterose.ac.uk/131223/

Version: Accepted Version

Article:
Baran, JD, Kepaptsoglou, D, Molinari, M et al. (5 more authors) (2016) Role of Structure and Defect Chemistry in High-Performance Thermoelectric Bismuth Strontium Cobalt Oxides. Chemistry of Materials, 28 (20). pp. 7470-7478. ISSN 0897-4756

https://doi.org/10.1021/acs.chemmater.6b03200

(c) 2016, American Chemical Society. This document is the Accepted Manuscript version of a Published Work that appeared in final form in Chemistry of Materials, copyright © American Chemical Society after peer review and technical editing by the publisher. To access the final edited and published work see
https://doi.org/10.1021/acs.chemmater.6b03200

Reuse
Items deposited in White Rose Research Online are protected by copyright, with all rights reserved unless indicated otherwise. They may be downloaded and/or printed for private study, or other acts as permitted by national copyright laws. The publisher or other rights holders may allow further reproduction and re-use of the full text version. This is indicated by the licence information on the White Rose Research Online record for the item.

Takedown
If you consider content in White Rose Research Online to be in breach of UK law, please notify us by emailing eprints@whiterose.ac.uk including the URL of the record and the reason for the withdrawal request.

White Rose university consortium
Universities of Leeds, Sheffield & York

eprints@whiterose.ac.uk
https://eprints.whiterose.ac.uk/

The Role of Structure and Defect Chemistry in High-Performance Thermoelectric Bismuth Strontium Cobalt Oxides

Jakub D. Baran[1], Demie M. Kepaptsoglou[2], Marco Molinari[1], Nuth Kulwongwit[3], Feridoon Azough[3], Robert Freer[3], Quentin M. Ramasse[2] and Stephen C. Parker[1*]

[1]*Department of Chemistry, University of Bath, Claverton Down, Bath BA2 7AY, U.K.*

[2]*SuperSTEM Laboratory, SciTech Daresbury Campus, Daresbury WA4 4AD, U.K.*

[3]*School of Materials, University of Manchester, Manchester, M13 9PL, U.K.*

Corresponding author email: S.C.Parker@bath.ac.uk

Abstract

$[Bi_{0.87}SrO_2]_2[CoO_2]_{1.82}$ (BSCO) is one of the best *p*-type thermoelectric oxides but its structural and electronic properties are still little understood. BSCO is a misfit-layered compound consisting of an incommensurate stacking of hexagonal CoO_2 and double rock-salt $BiSrO_2$ layers. Here we combine experimental and computational approaches to investigate its crystallographic and electronic structure as well as thermoelectric transport properties. Considering different approximations for the subsystems stacking we present a structural model that agrees well with both bulk and atomic-scale experimental data. This model, which suggests a level of Bi deficiency in the rock-salt layers, is then used to discuss the material's electronic, magnetic and transport properties. We show that Bi-deficiency leads to a band-gap opening and increases *p*-type electronic conductivity due to the formation of Co^{4+} species that serve as itinerant holes within the predominantly Co^{3+} framework of the CoO_2 layer. We validate these predictions using electron energy loss spectroscopy in the scanning transmission electron microscope. The relationship between the hole-doping mechanism and the changes of the local structure (in particular the level of Bi deficiency) is evaluated. The reliability of the simulations is supported by the calculated temperature dependence of the Seebeck coefficient, in good agreement with experimental measurements.

1. Introduction

Thermoelectric (TE) devices convert heat into electricity and represent an important route for green technologies. They have the potential for making an impact in many fields, such as portable devices (medical applications) and smart grid systems (coupled with batteries and photovoltaics). Metal oxides possess several advantages over traditional thermoelectric (TE) materials including low price, non-toxicity, chemical and thermal stability at high temperature.[1-4] Furthermore, the chemical richness of their structures ensures that their properties are highly tuneable. However, due to their normally-low electronic conductivity, they are often neglected for their potential use in TE modules.[5, 6] Furthermore, an efficient TE device requires both a *p*-type and *n*-type material, which adds to the materials design challenge.[7] The discovery of the layered cobalt oxides, like sodium cobaltate Na_xCoO_2, calcium cobaltite $[Ca_2CoO_3]_{0.62}CoO_2$ (CCO) and bismuth strontium cobaltite $[Bi_{0.87}SrO_2]_2[CoO_2]_{1.82}$ (BSCO) has completely changed the traditional understanding of oxide materials in TE research.[8, 9] These layered materials exhibit high electrical conductivity (σ) and Seebeck coefficient (*S*) and low thermal conductivity (k_l).[8] In the TE community, the figure of merit ($ZT= T*\sigma*S^2 / k$) is used to express the efficiency of a TE material. For example, Na_xCoO_2 has σ≈200 μΩcm, S≈+100 μVK^{-1} and k_l≈2.0 $Wm^{-1}K^{-1}$[10] which give it a figure of merit (ZT) of 1.2 at 800 K while its power factor ($PF= \sigma*S^2$) of 50 $\mu Wcm^{-1}K^{-2}$ exceeds that of state-of-the-art thermoelectric Bi_2Te_3 at room temperature.[11] The high efficiency of these layered materials is due to a combination of several factors including glass-like low thermal conductivities due to their incommensurate crystal structure, high electronic conductivity arising from charge reorganization between the material subsystems[12] and a high Seebeck coefficient originating from strong electron correlation and spin-entropy relation.[13-15] Although much experimental and theoretical work has been devoted to the understanding of structural and electronic properties of Na_xCoO_2[10, 11, 16] and CCO,[13, 17-21,22-24] these properties are, so far, little understood for BSCO[25-27], which contains no elements that are scarce or considered seriously harmful and has a working temperature up to 1000 K [25] and is thus arguably one of the most promising thermoelectric oxide materials. To some extent, this can be ascribed to the challenges posed by the incommensurate crystal structure, the complex defect chemistry and the strong electron correlation due to the presence of Bi and Sr species.

Accurate information on the crystal structure and the resulting electronic properties of a material is of paramount importance for understanding and predicting TE properties reliably as macroscopic quantities like Seebeck coefficient and electronic conductivity in $[Bi_{0.87}SrO_2]_2[CoO_2]_{1.83}$ are directly related to the electronic states in the vicinity of the Fermi level and are defined by the crystal structure of a material. Fortunately, density functional theory electronic band-structure calculations combined with the Boltzmann transport theory provide an invaluable route for this task, especially when

combined with experimental techniques such as X-ray diffraction (XRD) and scanning transmission electron microscopy (STEM), which can probe the material at different length scales and be used to validate the theoretical predictions. Here, we initially discuss the stability of possible structural model approximations for the BSCO incommensurate structure inferred from experimental observations at the atomic scale of the stacking arrangement of the two sub-systems. We compare the electronic and magnetic properties of stoichiometric and Bi-deficient composition and discuss the dependence of these properties on the Bi stoichiometry. We finally combine the DFT band-structure with Boltzmann transport theory to calculate temperature dependence of the Seebeck coefficient and compare it to experimental thermoelectric data.

2. Results and Discussion

Structural parameters

BSCO was for the first time synthesised and studied by X-ray diffraction by Leligny *et al.*[27, 28] They showed that this compound is composed of CdI_2-type $[CoO_2]$ layers (hereafter referred to as COL) with edge-sharing CoO_6 octahedra as in Na_xCoO_2, which are separated by rock-salt (hereafter referred to as RS) type $[BiSrO_2]$ layers. Due to short Bi-Bi distance between the BiO layers it was suggested that some of the Bi sites should be vacant making the RS layers bismuth deficient $[Bi_{1-x}O]$. The overall stoichiometry of BSCO has thus been expressed as $[Bi_{0.87}SrO_2]_2[CoO_2]_{1.82}$.[26, 27] According to existing literature X-ray data, the Bi deficiency results in the formation of two regions in the BiO layers: one which extends over several interatomic BiO distances and can be considered as ordered and stoichiometric, whereas the other is Bi-deficient, narrow and disordered[28] but this has thus far not been confirmed at the atomic-scale.

The RS layer is sandwiched between two COL along the *c* crystal direction. Both subsystems share the same *a* and *c* lattice parameters, but they are incommensurate along the *b* axis. The incommensurate stacking structure of BSCO can be approximated by using a supercell where the ratio between RS and CoO_2 unit is parameterised using an integer number *n*: $[Bi_4Sr_4O_8]_n[Co_4O_8]_{(2n-1)}$. The periodicities of the RS and COL subsystems are expressed as $b_{RS} = b/n$ and $b_{COL} = b/(2n-1)$, where *b* is the unit cell length along the *b* axis. We note that the structural models of BSCO differ from those of calcium cobaltite (CCO) $[Ca_2CoO_3][CoO_2]_{1.62}$, another incommensurate oxide thermoelectric material, where the ratio of COL/RS forms two consecutive Fibonacci numbers *i.e.,* (*F(n+1)/F(n) = 5/3, 8/5, 13/8*, …).[19] In the case of BSCO, the *n=6* approximant (also denoted as the 6/11 system) corresponds to an overall stoichiometry of $[BiSrO_2]_2[CoO_2]_{1.83}$ and is therefore the closest to the experimentally-determined composition of the material used here: $[Bi_{0.87}SrO_2]_2[CoO_2]_{1.82}$.[26, 28] We will

thus focus on the 6/11 model in what follows, although for completeness we also considered the case for *n=5* (5/9 system) corresponding to a stoichiometry of $[BiSrO_2]_2[CoO_2]_{1.80}$. A detailed comparison between the 5/9 and 6/11 models is included in the Supplementary Information (SI) provided.

Figure 1 shows the primitive unit cell of the 6/11 model of BSCO along the [100], [110] and [010] crystallographic directions, where six BiSrO (RS) units can be distinguished clearly in the [100] crystal direction (Figure 1a).

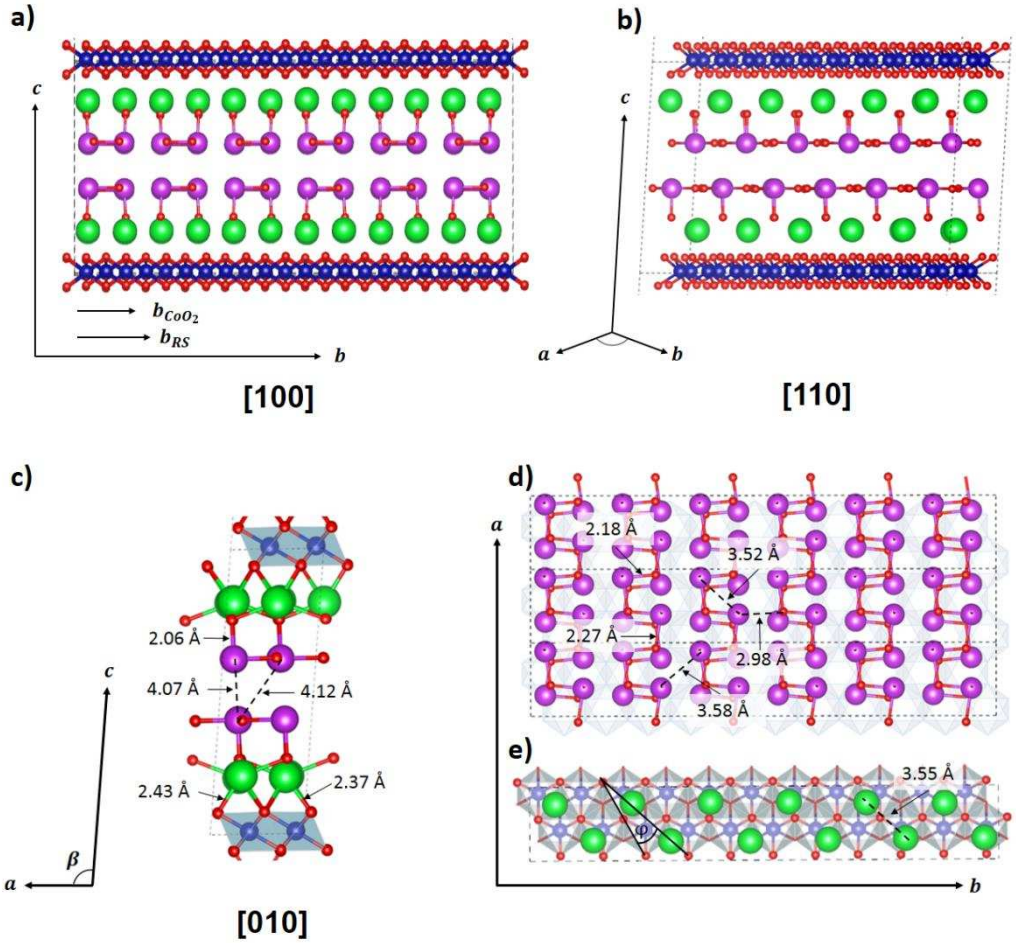

Figure 1: PBE*sol+U* optimized 6/11 unit cell along a) [100] and b) [110] projection; c) [010] projection with selected bond lengths; d) view of the BiO chains in the (*a*-*b*) plane; e) Sr position with respect to the CoO_2 layer in the (*a*-*b*) plane. The green, blue, red and pink balls correspond to Sr, Co, O and Bi atoms, respectively.

The electronic and structural properties of the BSCO models were studied *via* density functional theory calculations (DFT). A number of exchange-correlation functionals was tested however, we will describe here the results as obtained with the PBEsol+*U* functional. This is because: (i) the PBEsol+*U* yields the best agreement between experimental and calculated lattice constants; (ii) it has been shown that the inclusion of the Hubbard *U* parameter improves the description of the electronic, phonon and transport properties when compared to experiments for other similar misfit-layered cobalt oxides.[12, 29, 30] The detailed description of methods and the calculated parameters with other

functionals are provided in the SI. Selected calculated structural parameters are highlighted in Figure 1c-e. The Sr ions occupy the rows between adjacent triangles of the COL oxygens and have a zig-zag like pattern along the [100] crystal direction (Figure 1e). The SrO bond length of around 2.4 Å suggests a strong interaction between Sr and O as in the rocksalt SrO structure (Figure 1c). In contrast, the interlayer Bi-Bi distance is around 4.10 Å, which is close to the sum of two van der Waals (vdW) radii for Bi (2 x 2.07 = 4.14 Å),[31] suggesting a weak interaction between successive BiSrO layers, as also suggested by Leligny *et al.* from their experimental data.[28] In the case of the 6/11 model, the DFT structural optimisation suggests that BiO chains are formed along the [010] crystal direction (Figure 1d). There are two BiO distances within these chains, a shorter one at 2.18 Å and a longer one of 2.27 Å. The Bi-Bi distances between adjacent chains is approximately 3.50 Å, shorter than the sum of the vdW radii for Bi but longer than the sum of covalent radii of 2.92 Å, indicating an intermediate bonding type between covalent and vdW. The calculated misfit angle φ of ≈20˚ (Figure 1e) agrees well with the experimentally-measured value of ≈17˚of Maki *et al.*[32]

These optimised structural parameters were used to refine new experimental X-ray diffraction data obtained at the Diamond Light source, station I11: Figure 2. For comparison, the structural parameters provided by Leligny *et al.*[26] were also used to refine the same data: see SI for details on the refinement procedure. The full-pattern refinement using both sets of structures demonstrated good fitting parameters, with R-weighted-patterns (Rwp) of 12.67 and 9.49, and a goodness-of-fit (GOF) of 1.34 and 1.01 for the cases of the structure provided by Leligny *et al.*[26] and the present 6/11 DFT model, respectively. This would indicate an overall better fit of the 6/11 DFT model compared to that of Leligny's. However, some of (0 0 l) family of reflections especially the (0 0 10) do not fully match the experimental intensity. This is the case for both the Leligny and our DFT-minimized structures (albeit to a lesser degree for the latter), and may be due to the preferred orientation of the plate-shaped grains causing unreasonably sharp peaks beyond the scope of mathematical compensation.

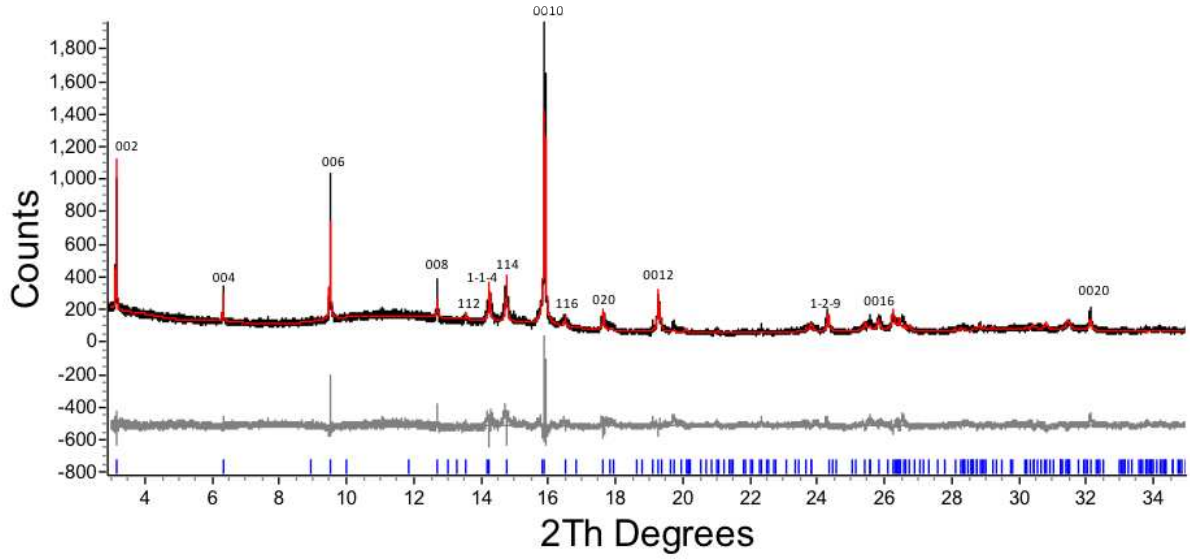

Figure 2: Full spectrum Rietveld refinement of BSCO samples using DFT structure. The black line is the experimental data, the red line is the mathematical fit, and the grey line shows the difference between experimental and calculated profiles. The blue vertical lines are the calculated reflections.

Although the newly-calculated DFT 6/11 structural model fits well the experimental XRD pattern, X-ray-diffraction-based techniques only provide information about the overall bulk structure and it is known in these misfit layered compounds that local modulations occur at the local, atomic-scale: for instance, atomic-resolution imaging of $Ca_3Co_4O_9$ was instrumental in confirming the presence of a strong modulation of the CoO columns in the (001) direction.[22] Atomically-resolved high-angle annular-dark-field (HAADF) STEM imaging (see SI section for experimental and technical details) was thus used to directly observe of the local structure of BSCO and to confirm the stacking arrangement of the RS and COL subsystems. A representative image (additional data is provided in the SI), acquired along the [110] zone axis, is shown in Figure 3. In this orientation, because of the large Bi–Bi or Sr-Sr atomic distances (3.52 Å and 3.55 Å, respectively, as predicted in our calculations, and a model of the structure in this projection in Figure 1b), it is possible to resolve the positions of Bi and Sr in the RS layers and therefore the relative arrangement of the RS layers with respect to the COL. Due to the dependence of the contrast in HAADF STEM images[33] on the average atomic number Z as $\sim Z^{1.7}$, the brighter spots observed in the image can be straightforwardly interpreted as corresponding to the heavier Bi (Z_{Bi}=83) columns and smaller spots with lesser intensity represent the Sr (Z_{Sr}=38) columns. In this orientation the Co (Z_{Co}=27), atomic column positions cannot be individually resolved, but rather appear as continuous lower intensity lines between the RS layers. Spatially-resolved chemical maps of the structure are presented in Figure S1 of the supplementary material provided for confirmation of this structural assignment and show an excellent agreement between the calculated and observed structures.

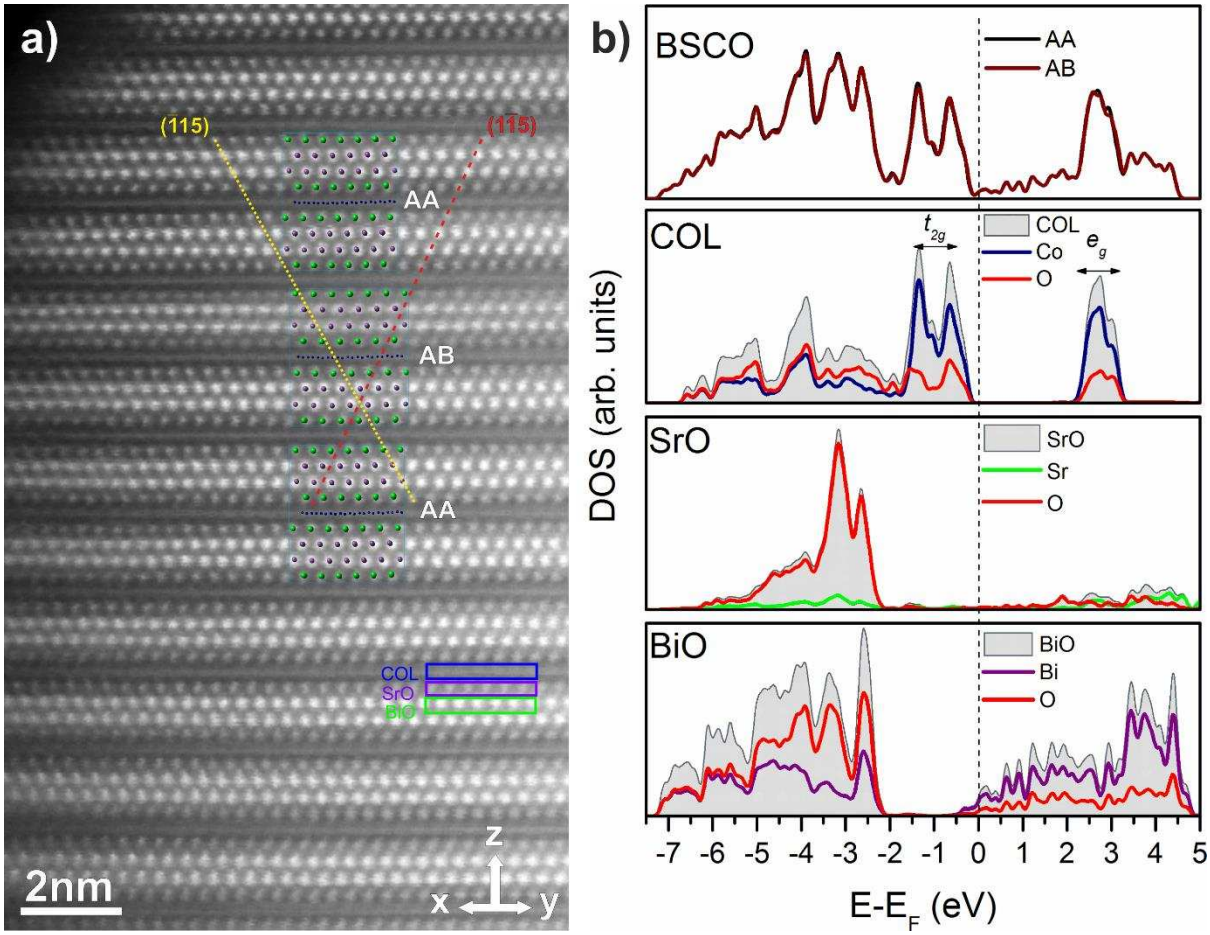

Figure 3: a) HAADF STEM image of a BSCO crystal acquired along the [110] orientation and ball models of the BSCO structure ('AA' and 'AB' stackings, respectively) superimposed on the image (Bi is represented by purple balls, Sr by green balls, Co by blue balls). The directions of the $(\bar{1}15)$ and $(1\bar{1}5)$ planes are marked by the dotted yellow and dashed red lines, respectively. The change in RS stacking is annotated on the figure. b) PBEsol+*U* DOS for the total for AA and AB stacking (BSCO), projected on Co and O of COL (COL), projected on Bi and O of BiO layer (BiO) and projected on Sr and O of the SrO layer (SrO). The Fermi level is set up at 0 eV.

Careful examination of the image in Figure 3a reveals however the presence of two different stacking arrangements of the RS units (named hereafter 'AA' and 'AB' respectively), indicated by ball and stick models superimposed on the HAADF image in Figure 3a at the position where the RS sub-system is shifted by half-a-unit-cell in the x-y plane compared to the 'regular', or 'AA' stacking. A more detailed description of the structure of this stacking fault is provided in the SI. The calculated energy difference between the relaxed structures for the two stacking variants is only 5 meV per Co atom, with the unfaulted stacking (as seen across most of Figure 3a) being more stable. This indicates that both these structural motifs can be present within the material and that the formation of these stacking faults is relatively favourable from an energetic point of view. The presence of a large density of such stacking faults, possibly leading to extended domains with different stacking sequences of the RS layers in BSCO and the frequency of their occurrence are to be investigated in detail elsewhere. We note however that even a moderate density of such stacking faults in the samples is unlikely to affect

the refinement of the experimental X-ray diffraction patterns and improve the match to available structural data. Nevertheless, a possible structural disorder along the *c*-axis caused by the different arrangements of consecutive BSCO layers could be partially responsible for the low lattice thermal conductivity of the material, and having unambiguously observed the presence of these stacking domains in the material it is therefore interesting to consider possible differences in electronic and/or transport properties between the models.

Electronic Structure

Analysis of the temperature-dependent resistance and magnetoresistance properties of single crystalline samples of BSCO suggests it has a semiconductor-like character and weak electron localization related to the co-existence of Co^{3+} and Co^{4+} in COL, which results in a finite magnetic moment of some of the Co species.[34] Moreover, it is known that a metal-insulator transition takes place at approximately 200 K, which indicates the existence of a pseudo-gap around the Fermi level, whose origin is ascribed to a strong correlation between the electrons.[25] The transport properties of a *p*-type semiconductor like BSCO directly depend on the topology of the electronic states in the vicinity of valence band (VBM) maxima. Thus in order to gain insights into the electronic properties of the material, we evaluate the total and site-projected electronic density of states (DOS) of BSCO using the 6/11 model we have now established and optimised, considering for completeness the two different types of stacking sequences observed experimentally, which we denote as AA and AB stacking. The site-projection is achieved by averaging contributions to the DOS over all states corresponding to all atoms of a given species. As shown in Figure 3b the DOS for AA and AB stacking is visually indistinguishable, which indicates that changes in stacking of the BSCO layers should not affect the electronic properties of the system. In both models the Fermi level is located close to the sharp peak originating from Co-*d* states of the COL. The VB is seen to be mostly composed of Co-*3d* and O-*2p* hybridized states (Figure 3b, COL), whereas the conduction band (CB) comprises Bi and O states of the BiO layer (Figure 3b, BiO). From 2 eV to around 3.5 eV above the Fermi level there is a pronounced peak of the anti-bonding Co and O states (Figure 3b, COL). COL states are split into t_{2g}-e_g states (Figure 3b, COL) as in the octahedral crystal field. The t_{2g} orbitals are fully occupied which implies that all Co ions are in a +3 oxidation state for this non-deficient system, whereas e_g states are empty. The states from the SrO layer (Figure 3b, SrO) lie in the energy region of -2 to -6 eV below the Fermi level and are composed mostly of O-*2p* states. Since there is no energy gap for the non-Bi deficient system as shown in the DOS in Figure 3b, the electrical conductivity of such a material would be controlled by defect chemistry as described below for Bi deficient systems. Note that the contributions to the PDOS in Fig. 3b have been scaled for greater visibility. The unscaled PDOS is shown in Figure S7b. Moreover, in BSCO Bi atoms are in asymmetric environment, which allows the formation of the

Bi- lone pairs.[35, 36] This is in line with calculated electron localization function plots (see Figure. S8), where the Bi- lone pairs are visible and appear to be located at the corner of the octahedra between BiO layers. Given the very low energy cost associated with the formation of an AB stacking fault, and the virtually identical resulting electronic structure, we will now only consider the more typical AA stacking.

Bi-deficiency and Co valence

According to experimental evidence, BSCO is a Bi-deficient material with the overall stoichiometry of $[Bi_{0.87}SrO_2]_2[CoO_2]_{1.82}$.[26, 27] It has been assumed that Bi deficiency occurs in order to reduce stress in the BiO layers originating from close Bi-Bi distances.[26] In the following section, we discuss the effect of Bi deficiency on the electronic, magnetic and transport properties of BSCO. We have investigated Bi-deficient structures with stoichiometries of $[Bi_{0.96}SrO_2]_2[CoO_2]_{1.83}$, $[Bi_{0.91}SrO_2]_2[CoO_2]_{1.83}$ and $[Bi_{0.87}SrO_2]_2[CoO_2]_{1.83}$ that resulted from a random removal of one, two and three Bi atoms per unit cell of the 6/11 structural model containing a single stacking type of the RS sub-system (half of what we denote the AA stacking), respectively. Increasing Bi deficiency induces band gap opening and the formation of a magnetic moment in the unit cell (Table 1).

Table 1: Band-gap in eV and total magnetic moment in Bohr/unit cell for non- and Bi-deficient structures of BSCO as resulted from PBEsol+U calculations.

Composition	Band Gap (eV)	Magnetic Moment (μ_B)
$[BiSrO_2]_2[CoO_2]_{1.83}$	0.013	0
$[Bi_{0.96}SrO_2]_2[CoO_2]_{1.83}$	0.284	1.23
$[Bi_{0.91}SrO_2]_2[CoO_2]_{1.83}$	0.350	2.04
$[Bi_{0.87}SrO_2]_2[CoO_2]_{1.83}$	0.612	4.70

Figure 4 reveals the spatial relationship between the formation of a localized magnetic moment and the presence of Bi vacancy defects in the case of $[Bi_{0.87}SrO_2]_2[CoO_2]_{1.83}$ (corresponding to the removal of 3 Bi atoms per unit cell of the non-deficient 6/11 model). The magnetic moment appears to be localized on the Co species of COL (Figure 4a) immediately adjacent to the vacant Bi site. A schematic of that CoO_6 octahedron in the deficient case (*i.e.* the octahedron on which there is a localized magnetic moment) is shown in Figure 4b, and compared to the non-Bi-deficient case. The average Co-O bond distance for the latter is 1.908 Å, significantly longer than for the Bi-deficient case of 1.879 Å. Therefore our results provide a direct link between Bi sub-stoichiometry and hole-doping in COL. In the Bi-deficient case, the CoO_6 octahedra situated relatively close to the vacant Bi sites and on which a magnetic moment is created locally are distorted compared to the other octahedra. This

structural modification can be interpreted as a being the result of an increased Coulombic attraction between Co and O. The shortened Co-O bond-lengths in turn suggest that these Co ions which are strongly attracting the surrounding O ions possess a higher valence and are therefore Co^{4+} rather than Co^{3+} as would be the case for the undistorted octahedra.

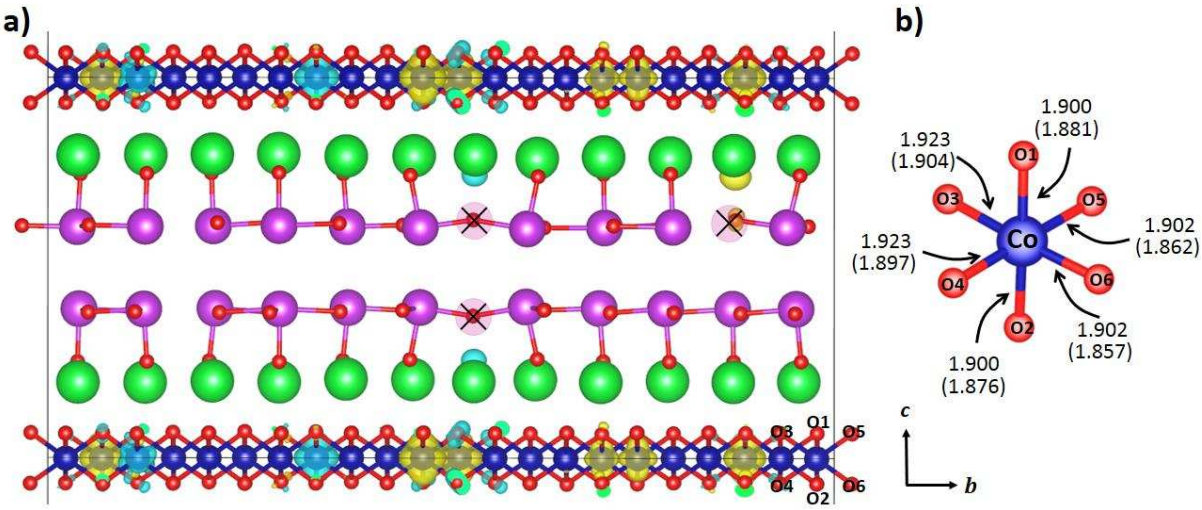

Figure 4: a) Structure of $[Bi_{0.87}SrO_2]_2[CoO_2]_{1.83}$. The Bi vacant sites are indicated by the crossed circles. The yellow/blue area in COL represents +/- spin density isosurface of 0.01 μ_B/a_0, respectively and indicates Co^{4+} ions b) a local environment of the of Co^{4+} (in parenthesis) as averaged from the species on which localized magnetic moment is present, and Co^{3+} with zero magnetic moment.

This suggestion was directly validated experimentally through atomically-resolved electron-energy-loss spectroscopy. The valence of Co species can be estimated by analysing the Co $L_{2,3}$ electron energy loss near edge fine structure (ELNES) and more specifically by determining the intensity ratio between the L_3 and L_2 peaks, also often called white lines, which result from transitions from the $2p_{3/2}$ and $2p_{1/2}$ Co electronic states to the continuum under excitation by the incoming electron beam. Figure 5a shows the Co $L_{2,3}$ edge averaged from a number of adjacent pixels from a spectrum image (see Figure S2a where the full dataset is presented) over an area of COL similar to that indicated by the blue box on Figure 3a. Further details of the processing are provided in the SI. The Co L_3:L_2 intensity ratio was estimated from this spectrum to be 2.35±0.1, corresponding to an approximate Co valence state in the COL layers between +3 and +4.[37] As the Bi vacancies are not expected to be ordered through the thickness of the sample, this result is thus perfectly consistent with a number of hypervalent Co sites, resulting in an overall valence slightly higher than the +3 expected from a non-Bi-deficient structure.

Furthermore, Figure 5b shows background-subtracted O *K* spectra extracted and averaged from the COL (over an area similar to that indicated by a blue box on figure 3a), SrO (purple box) and BiO (green box) layers in the structure, respectively. The O *K* ELNES shows three distinct features, which vary depending on which atomic layer the spectrum is extracted from; peak A at ~532 eV, B at~

537.5 eV and peak C at ~544.2 eV. The O K spectrum from the COL layer shows sharp A and C peaks, with a lower B peak intensity. In the SrO layer peak B shifts to lower energies and its intensity increases with respect to peaks A and C. On the left of the main A peak in the COL layer, some additional pre-peak intensity – labelled as A_1, can be observed; a similar feature has been previously observed the CoO_2 layers of CCO[22] and was attributed to hybridised O *2p* and Co^{4+} states, consistent with the presence hypervalent Co sites in the COL layer inferred from our theoretical calculations. In the BiO layer peak A broadens and shifts to higher energies, while its intensity drops significantly, as does that of peak C. In a single electron approximation the EELS O *K* edge is directly related to the density of empty states in the structure: these atomically-resolved spectral differences can be compared to the calculated DOS projected onto the relevant atomic layers to validate our theoretical model: Figure 5c.

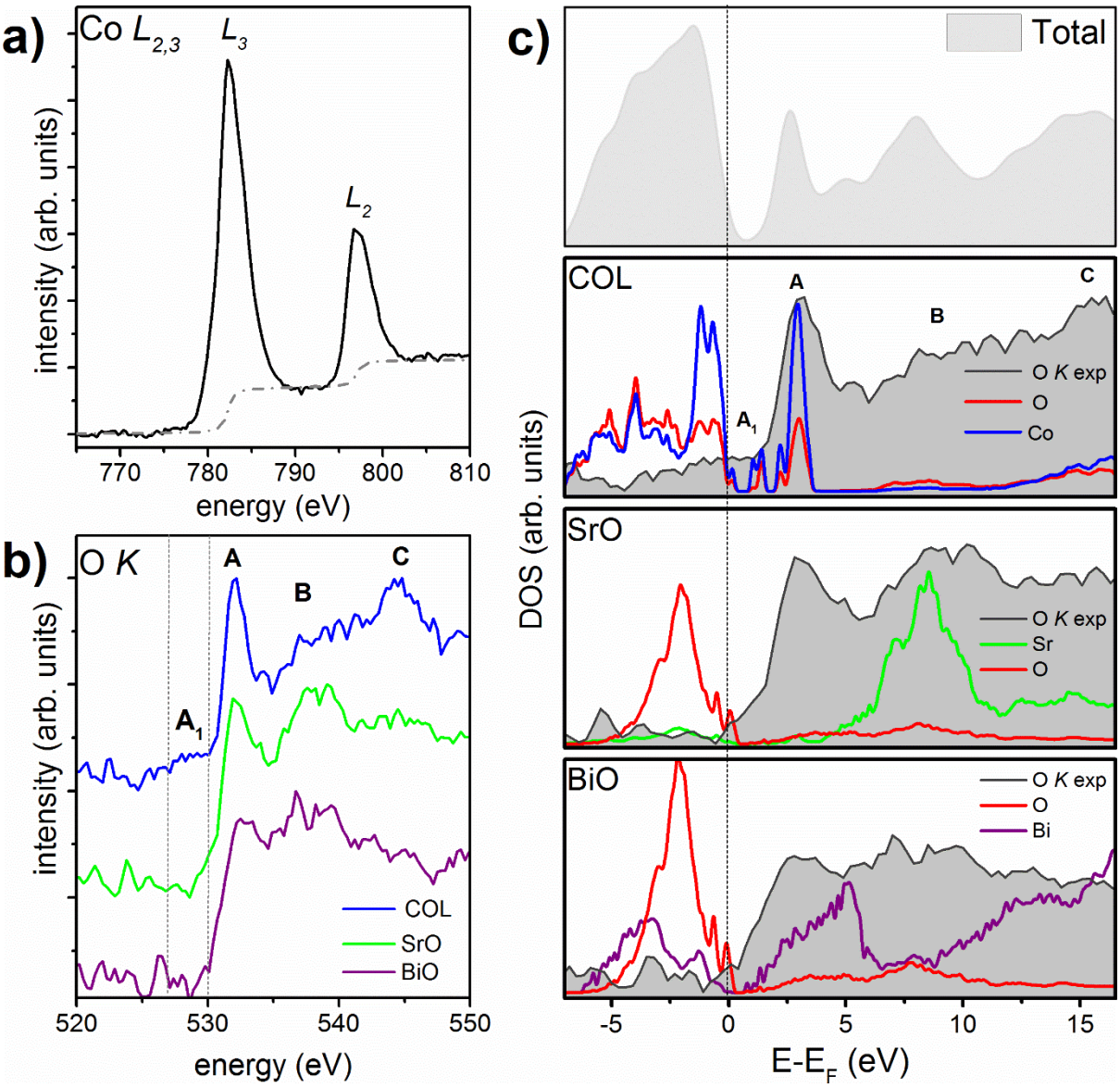

Figure 5: a) Background subtracted Co $L_{2,3}$ EEL spectrum extracted from the COL layer in a region similar to that marked in Figure 3a showing the double arctan EELS background used for the estimation of the L_3:L_2 intensity ratio. b) Background-subtracted O *K* EEL spectra (un-processed data) corresponding to layers similar to those

marked in Figure 3a. c) Total calculated DOS of the B-deficient $Bi_{0.87}SrO_2]_2[CoO_2]_{1.83}$ and site-projected DOS on the Co and O of COL, Sr and O of the SrO layer and projected on Bi and O of BiO layer, as labelled. The Fermi level is set up at 0 eV. The p-DOS is plotted against the experimental O *K* edges for the corresponding layers (as defined in Figure 3a). For reading clarity, the experimental spectra were rigidly-translated to the site projected p-DOS; no stretching of the energy axis was applied. Spin-up and -down channels in the calculated p-DOS are added up here.

Figure 5c shows the experimental EEL spectra overlaid onto the relevant site-projected DOS for the COL, SrO and BiO layers, respectively, calculated in the case of the Bi-deficient $[Bi_{0.87}SrO_2]_2[CoO_2]_{1.83}$ model, and reveal an excellent agreement. The sharp A peak observed in the O *K* ELNES of the COL layers can be clearly seen to arise from Co-*3d* and O-*2p* hybridized states (~3.5 eV above the Fermi level in the COL p-DOS), while the A_1 pre-peak intensity lying ~1 eV above the Fermi level is arising from the hybridization of the O-*2p* with the Co^{4+} states formed because of the presence of Bi vacancies in the structure. The emergence and downshift of the B peak in the SrO layer is due to Sr-*4d* and *O-2p* state overlap (~8 eV above the Fermi level in the SrO layer). In the BiO layer the upshift and broadening of the A peak corresponds to Bi-6p states hybridized with O-*2p* states.

Further analysis of the DOS of the Bi deficient-structure shows that the band gap-opening originates from the removal of the Bi states from the CB, see Figure 6a. The other important feature arising in this calculated DOS is the formation of localized Co states 0.5-1.5 eV above the Fermi level. This leads to a change in character of the CB from the predominantly BiO of the non-deficient system to Co-O of the deficient system. The evolution of the Co states with an increase of Bi deficiency is shown in Figure 6b. The increase in Bi deficiency leads to the Fermi level shifting deeper into the VB and the formation of the additional Co states increases systematically. There is a shift of the t_{2g} band deeper into the VB away from the highest occupied state as shown in Figure 6b. In addition, the Co cations in the COL have mixed valence, in which most of the Co ions are in +3 oxidation state with itinerant holes represented by Co^{4+} states, whose presence is confirmed experimentally by the appearance of shoulder A1 in the O *K* edge fine structure.

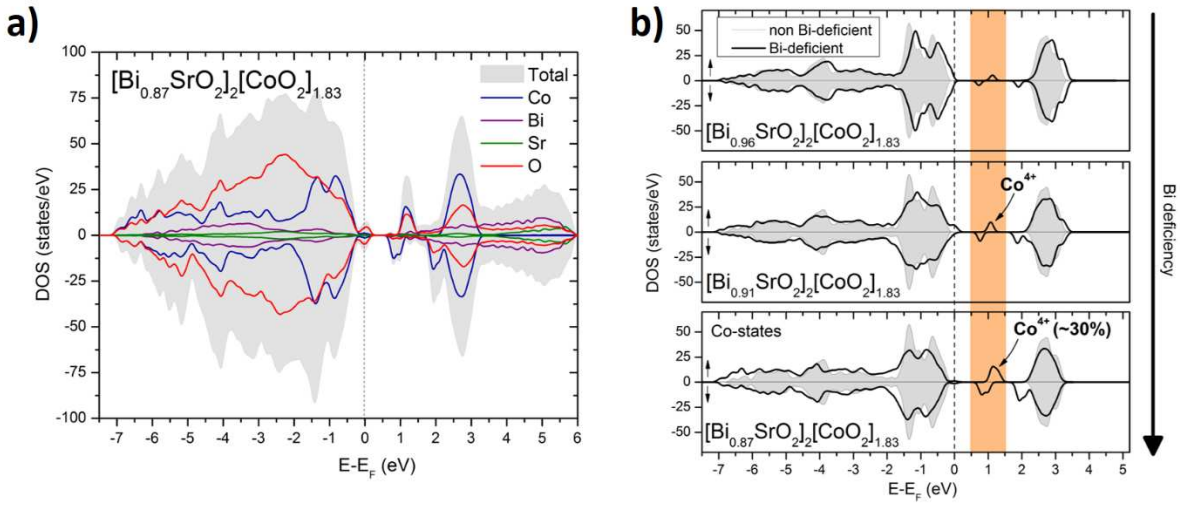

Figure 6: a) Full calculation results from the PBEsol+*U* DOS of $[Bi_{0.87}SrO_2]_2[CoO_2]_{1.83}$, considering the spin-degrees of freedom. b) Calculated PBEsol+*U* DOS for the Co states for the three Bi deficient structures compared to a non-deficient one. The highlighted region shows energy window above the Fermi level where Co^{4+} are formed.

The formation of the Co^{4+} can be conceptually explained by counting the formal oxidation state of the Co in COL and Bi in the BiO layer, assuming overall charge neutrality in the unit cell. The formal oxidation state of the Co in the pristine COL is 4+ (one Co is bonded to two oxygens of 2- charge), whereas Bi in the BiO layer of pristine BSCO would be of 2+ as one Bi is bonded formally to one oxygen. The Co cation has many electronic degrees of freedom and can be found in 2+,3+ and 4+ oxidation states, whereas the most stable oxidation state of Bi is 3+, e.g. in Bi_2O_3. In order to reach a 3+ oxidation state Bi transfers the excess change of an electron to COL, reducing Co^{4+} cations to Co^{3+} ones. In the case of the non-deficient system there are 24 Bi to 22 Co in the unit cell, and to keep the system charge neutral, formally, 22 of the Co should be turned to Co^{3+} while the remaining two take on a Co^{2+} valence. Such an intersystem charge transfer has been observed in the case of other misfit layered cobaltates and is intrinsically linked to their electronic and transport properties.[12, 22] With the removal of the one Bi atom assuming its 3+ oxidation state, all 22 Co can be of 3+ oxidation state and there is -1e charge left behind in the BiO layer. Due to the charge neutrality condition the excess of one negative charge in the BiO layer is compensated by the formation of one Co^{4+} (providing +1e charge) in the matrix of the Co^{3+}. This is in line with our calculations for, e.g., $[Bi_{0.96}SrO_2]_2[CoO_2]_{1.83}$ where one Bi was removed from the unit cell and we predicted the formation of the one localized Co site with a magnetic moment of ~ $1\mu_B$ as shown in Table 1. With a further increase of the Bi deficiency more Co^{4+} are formed in the COL layer as shown in Figure 6b corresponding to additional states localised in the region between +0.5 to +1.5 eV above the Fermi level. The formation of these states has a tremendous importance for the transport properties of the BSCO. The Co^{4+} localized magnetic moment increases the spin-entropy in the system and as a result enhances the Seebeck coefficient.[13] The predicted concentration of the Co^{4+} in COL for $[Bi_{0.87}SrO_2]_2[CoO_2]_{1.83}$ (12% Bi sites defective, corresponding to the experimentally

determined stoichiometry of these samples) is 29.4%. A similar ratio of Co^{4+}/Co^{3+} was found for the other misfit layer cobalt oxides[14, 19] and this amount of Co^{4+} is in good agreement with the clear experimental evidence from the EELS, as much smaller concentrations would have a less visible impact on the L_3/L_2 ratio method used to determine the Co valence experimentally.

Transport properties

Finally, we turn to the thermoelectric transport properties of BSCO. Experimental measurements for BSCO whiskers have been carried out by Funahashi *et al.*[8, 25] finding a dimensionless thermoelectric figure of merit of above 1.1, which corresponds to a conversion efficiency of around 10% at 973 K in air.[25] The Seebeck coefficient was measured to be ~100 μV/K at 300 K and increased ~150 μV/K at 1000 K.[8] Providing a theoretical description of transport properties on the other hand has always been challenging due to the complexity of the phenomena that need to be taken into account.[38] It should also be noted that the calculated properties are for perfect single crystals while experimental samples inevitably contain different types of imperfections, such as impurities, extended defects and defect clustering, which strongly affect TE properties, in particular electron transport properties and are often beyond current modelling capabilities (due to the need to keep any calculation computationally tractable). Nevertheless, Figure 7 shows the calculated Seebeck coefficient averaged over all crystallographic directions as a function of the temperature for the non-Bi-deficient BSCO model (taken at the Fermi level *i.e.*, μ=0 eV) and for the experimentally-determined composition of $[Bi_{0.87}SrO_2]_2[CoO_2]_{1.83}$ (calculated at both μ=0 eV and μ=0.09 eV). Additional Seebeck coefficient measurements were also carried out on the experimental samples used for this study and are compared to the simulations: see SI for experimental details.

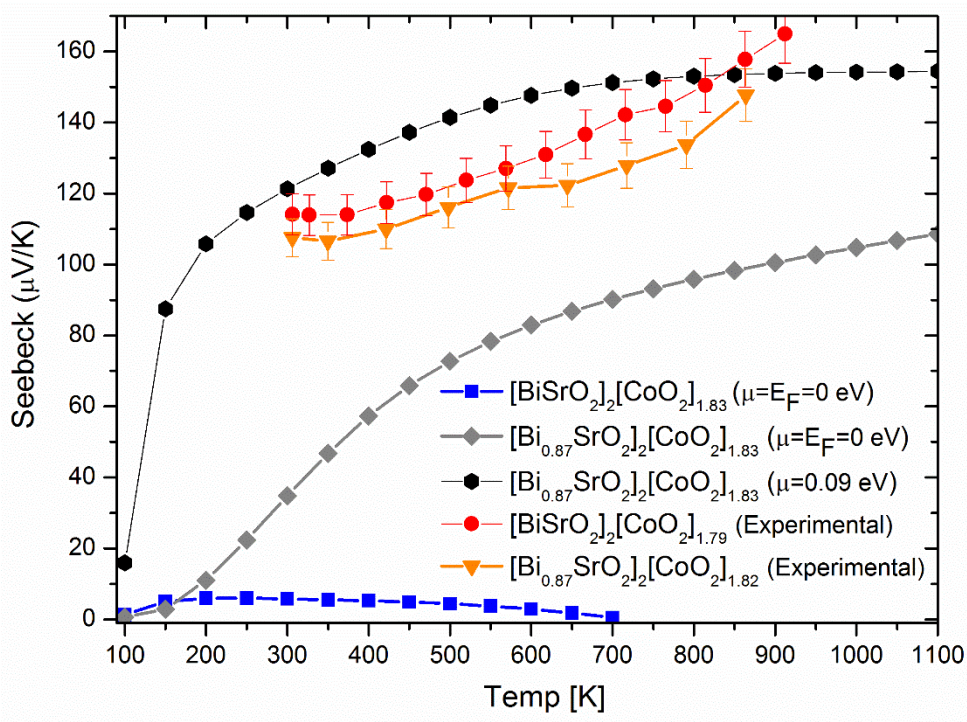

Figure 7: Calculated and experimental Seebeck coefficient for the non Bi-deficient and Bi-deficient BSCO.

Due to the metallic character of the non Bi-deficient system its predicted Seebeck coefficient is very low, demonstrating clearly that the experimental composition must contain Bi vacancies as the measured Seebeck values are far higher. For the system with Bi deficiency corresponding to the experimental composition of $[Bi_{0.87}SrO_2]_2[CoO_2]_{1.83}$ the calculated Seebeck coefficient increases with temperature, in line with the experimental measurements.[8] The calculated temperature dependence of the Seebeck coefficient as taken at the Fermi level (chemical potential μ=0 eV) corresponds to a carrier concentration of $1.47*10^{20}$ e/cm^{-3} at 300 K, which is in agreement in terms of order of magnitude with, albeit slightly lower than, the values measured experimentally. However, if it is taken at μ=0.09 eV it would correspond to a carrier concentration of $1.96*10^{21}$ e/cm^{-3} at 300 K, which is this time in excellent numerical agreement with the experimental measurements both from the literature[8] and from the present samples: see Figure 7. Such a small shift of chemical potential μ from the Fermi level can account for a slight difference between the experimental and theoretical composition of BSCO that has not been taken into account in our model. Note that the behaviour of the calculated and experimental Seebeck coefficient differs: the experimental coefficient increases linearly with temperature, while the calculated values asymptotically reach a limit of 155 μV/K at high temperature from which a plateau is reached. The observed difference in trends can be explained by the sensitivity of the calculated Seebeck coefficient to the composition of BSCO. Our calculations show therefore the sensitivity of the calculated Seebeck coefficient to the structural composition and show that Bi deficiency not only decreases strain in the BiO layer but is essential to achieve its high transport

properties while Bi vacancies are also expected to act as scattering centres reducing thermal conductivity of the compound.

3. Conclusions

We have investigated the structural, electronic and transport properties of the misfit-layered BSCO thermoelectric material through a combination of experimental and theoretical techniques. We present a structural model for this complicated material that agrees well with the X-ray and electron microscopy data and discuss it in details. We show evidence for the presence of stacking faults, finding that changes in the relative arrangements of the CoO_2 and BiSrO layers can easily arise as their formation requires a very low energetic cost. Furthermore, Bi deficiency has been found to have a paramount importance on the electronic, magnetic and transport properties of BSCO. It was shown to lead to the hole-doping of the CoO_2 layer, for which we present direct experimental evidence through atomic-layer-resolved electron energy loss spectroscopy. Our theoretical modelling then shows how these atomic-scale structural and electronic structure modifications are in turn responsible for the high positive Seebeck coefficient of the material measured experimentally. This provides another step in understanding this fascinating material, which should be of great benefit in future design of oxide thermoelectric materials that are composed of inexpensive and abundant elements.

Supporting Information

Supporting information is available free of charge, and includes computational methodology, details about experimental procedures, additional microscopy and structural data, as well as a theoretical comparison between structural approximants for BSCO.

Notes

The authors declare no competing financial interest

Acknowledgements

This work was funded by EPSRC Programme grants EP/K016288/1 and EP/I03601X/1, and the following EPSRC awards, EP/J000620, EP/K022156, EP/L014068, EP/K022156:. Computations were run on ARCHER through the Materials Chemistry Consortium funded by EPSRC grant number EP/L000202 and the STFC Hartree Centre (Daresbury Laboratory, UK) High Performance Computing facilities. We also thank the EPSRC grant number of EP/16366230 for providing the microscope time. The SuperSTEM Laboratory is the U.K. National Facility for Aberration-Corrected STEM, supported by EPSRC.

References

(1) Srivastava, D.; Azough, F.; Freer, R.; Combe, E.; Funahashi, R.; Kepaptsoglou, D. M.; Ramasse, Q. M.; Molinari, M.; Yeandel, S. R.; Baran, J. D.; Parker, S. C., Crystal structure and thermoelectric properties of Sr-Mo substituted $CaMnO_3$: a combined experimental and computational study. *J. Mater. Chem. C* **2015,** 3, 12245-12259.

(2) Azough, F.; Freer, R.; Yeandel, S. R.; Baran, J. D.; Molinari, M.; Parker, S. C.; Guilmeau, E.; Kepaptsoglou, D.; Ramasse, Q.; Knox, A.; Gregory, D.; Paul, D.; Paul, M.; Montecucco, A.; Siviter, J.; Mullen, P.; Li, W.; Han, G.; Man, A. E.; Baig, H.; Mallick, T.; Sellami, N.; Min, G.; Sweet, T., Ba6−3x Nd8+2x Ti18O54 Tungsten Bronze: A New High-Temperature n-Type Oxide Thermoelectric. *J. Electron. Mater.* **2016,** 45, 1894-1899.

(3) Molinari, M.; Tompsett, D. A.; Parker, S. C.; Azough, F.; Freer, R., Structural, electronic and thermoelectric behaviour of $CaMnO_3$ and $CaMnO_{(3-\delta)}$. *J. Mater. Chem. A* **2014,** 2, 14109-14117.

(4) Srivastava, D.; Azough, F.; Molinari, M.; Parker, S. C.; Freer, R., High-Temperature Thermoelectric Properties of (1 − x) $SrTiO_3$ − (x) $La_{1/3}NbO_3$ Ceramic Solid Solution. *J. Electron. Mater.* **2015,** 44, 1803-1808.

(5) Gaultois, M. W.; Sparks, T. D.; Borg, C. K. H.; Seshadri, R.; Bonificio, W. D.; Clarke, D. R., Data-Driven Review of Thermoelectric Materials: Performance and Resource Considerations. *Chem. Mater.* **2013,** 25, 2911-2920.

(6) Chen, W.; Pohls, J.-H.; Hautier, G.; Broberg, D.; Bajaj, S.; Aydemir, U.; Gibbs, Z. M.; Zhu, H.; Asta, M.; Snyder, G. J.; Meredig, B.; White, M. A.; Persson, K.; Jain, A., Understanding thermoelectric properties from high-throughput calculations: trends, insights, and comparisons with experiment. *J. Mater. Chem. C* **2016,** 4, 4414-4426.

(7) Zhang, Y.; Stucky, G. D., Heterostructured Approaches to Efficient Thermoelectric Materials. *Chem. Mater.* **2014,** 26, 837-848.

(8) Funahashi, R.; Barbier, T.; Combe, E., Thermoelectric materials for middle and high temperature ranges. *J. Mater. Res.* **2015,** 30, 2544-2557.

(9) Yamauchi, H.; Sakai, K.; Nagai, T.; Matsui, Y.; Karppinen, M., Parent of Misfit-Layered Cobalt Oxides: $[Sr_2O_2]_qCoO_2$. *Chem. Mater.* **2006,** 18, 155-158.

(10) Kenjiro, F.; Tadashi, M.; Kazuo, N., High-Temperature Thermoelectric Properties of $Na_xCoO_{2-\delta}$ Single Crystals. *Jpn. J. Appl. Phys.* **2001,** 40, 4644-4647.

(11) Terasaki, I.; Sasago, Y.; Uchinokura, K., Large thermoelectric power in NaCo2O4 single crystals. *Phys. Rev. B* **1997,** 56, 12685-12687.

(12) Baran, J. D.; Molinari, M.; Kulwongwit, N.; Azough, F.; Freer, R.; Kepaptsoglou, D.; Ramasse, Q. M.; Parker, S. C., Tuning Thermoelectric Properties of Misfit Layered Cobaltites by Chemically Induced Strain. *J. Phys. Chem. C* **2015,** 119, 21818-21827.

(13) Masset, A. C.; Michel, C.; Maignan, A.; Hervieu, M.; Toulemonde, O.; Studer, F.; Raveau, B.; Hejtmanek, J., Misfit-layered cobaltite with an anisotropic giant magnetoresistance: $Ca_3Co_4O_9$. *Phys. Rev. B* **2000,** 62, 166-175.

(14) Isobe, M.; Onoda, M.; Shizuya, M.; Tanaka, M.; Takayama-Muromachi, E., Structure of the Monoclinic-Form Misfit-Layer Compound, $(Ca_{0.85}OH)_{2\alpha}CoO_2$ ($\alpha \approx 0.57822$). *J. Am. Chem. Soc.* **2007,** 129, 14585-14596.

(15) Wang, Y.; Sui, Y.; Ren, P.; Wang, L.; Wang, X.; Su, W.; Fan, H., Strongly Correlated Properties and Enhanced Thermoelectric Response in Ca_3Co_4−xMxO_9 (M = Fe, Mn, and Cu). *Chem. Mater.* **2010,** 22, 1155-1163.

(16) Singh, D. J., Electronic structure of $NaCo_2O_4$. *Phys. Rev. B* **2000,** 61, 13397-13402.

(17) Miyazaki, Y., Crystal structure and thermoelectric properties of the misfit-layered cobalt oxides. *Solid State Ion.* **2004,** 172, 463-467.

(18) Li, S.; Funahashi, R.; Matsubara, I.; Ueno, K.; Sodeoka, S.; Yamada, H., Synthesis and Thermoelectric Properties of the New Oxide Materials $Ca_{3-x}BixCo_4O_{9+\delta}$ ($0.0 < x < 0.75$). *Chem. Mater.* **2000,** 12, 2424-2427.

(19) Rébola, A.; Klie, R.; Zapol, P.; Öğüt, S., First-principles study of the atomic and electronic structures of misfit-layered calcium cobaltite using rational approximants. *Phys. Rev. B* **2012,** 85, 155132.
(20) Schrade, M.; Fjeld, H.; Finstad, T. G.; Norby, T., Electronic Transport Properties of $[Ca_2CoO_{3-\delta}]_q[CoO_2]$. *J. Phys. Chem. C* **2014,** 118, 2908-2918.
(21) Van Nong, N.; Pryds, N.; Linderoth, S.; Ohtaki, M., Enhancement of the Thermoelectric Performance of p-Type Layered Oxide $Ca_3Co_4O_{9+\delta}$ Through Heavy Doping and Metallic Nanoinclusions. *Adv. Mater.* **2011,** 23, 2484-2490.
(22) Yang, G.; Ramasse, Q.; Klie, R. F., Direct measurement of charge transfer in thermoelectric $Co_3Co_4O_9$. *Phys. Rev. B* **2008,** 78, 153109.
(23) Klie, R. F.; Qiao, Q.; Paulauskas, T.; Ramasse, Q.; Oxley, M. P.; Idrobo, J. C., Examining the structure and bonding in complex oxides using aberration-corrected imaging and spectroscopy. *Phys. Rev. B* **2012,** 85, 054106.
(24) Yang, G.; Ramasse, Q.; Klie, R. F., Direct measurement of Co-ion spin state transitions in $Ca_3Co_4O_9$ using variable-temperature electron energy-loss spectroscopy. *Appl. Phys. Lett.* **2009,** 94, 093112.
(25) Funahashi, R.; Shikano, M., $Bi_2Sr_2Co_2O_y$ whiskers with high thermoelectric figure of merit. *Appl. Phys. Lett.* **2002,** 81, 1459-1461.
(26) Leligny, H.; Grebille, D.; Perez, O.; Masset, A. C.; Hervieu, M.; Michel, C.; Raveau, B., A bismuth cobaltite with an intrinsically modulated misfit layer structure: $[Bi_{0.87}SrO_2][CoO_2]_{1.82}$. *Comptes Rendus De L Academie Des Sciences Serie Ii Fascicule C-Chimie* **1999,** 2, 409-414.
(27) Leligny, H.; Grebille, D.; Perez, O.; Masset, A. C.; Hervieu, M.; Raveau, B., A five-dimensional structural investigation of the misfit layer compound $[Bi_{0.87}SrO_2]_2[CoO_2]_{1.82}$. *Acta Crystallogr. Sect. B* **2000,** 56, 173-182.
(28) Grebille, D.; Muguerra, H.; Perez, O.; Guilmeau, E.; Rousseliere, H.; Funahashi, R., Superspace crystal symmetry of thermoelectric misfit cobalt oxides and predicted structural models. *Acta Crystallogr. Sect. B* **2007,** 63, 373-383.
(29) Rébola, A.; Klie, R. F.; Zapol, P.; Öğüt, S., Phonon and thermal transport properties of the misfit-layered oxide thermoelectric $Ca_3Co_4O_9$ from first principles. *Appl. Phys. Lett.* **2014,** 104, 251910.
(30) Wu, L.; Meng, Q.; Jooss, C.; Zheng, J.-C.; Inada, H.; Su, D.; Li, Q.; Zhu, Y., Origin of Phonon Glass–Electron Crystal Behavior in Thermoelectric Layered Cobaltate. *Adv. Funct. Mater.* **2013,** 23, 5728-5736.
(31) Mantina, M.; Chamberlin, A. C.; Valero, R.; Cramer, C. J.; Truhlar, D. G., Consistent van der Waals Radii for the Whole Main Group. *J. Phys. Chem. A* **2009,** 113, 5806-5812.
(32) Maki, M.; Takakura, S.-i.; Nishizaki, T.; Ichikawa, F., Microscopic adjustment of misfit strain and charge segregation in $[Bi_2Sr_2O_4]_{0.51}CoO_2$. *Phys. Rev. B* **2015,** 92, 165117.
(33) Pennycook, S. J.; Nellist, P. D.; Eds, *Scanning Transmission Electron Microscopy. Imaging and Analysis, 3rd ed*. Springer: New York: 2011.
(34) Dong, S. T.; Zhang, B. B.; Zhang, L. Y.; Chen, Y. B.; Yao, S. H.; Zhou, J.; Zhang, S. T.; Gu, Z. B.; Chen, Y. F., Metal-semiconductor-transition observed in $Bi_2Ca(Sr, Ba)_{(2)}Co_2O_8+\delta$ Single Crystals. *Appl. Phys. Lett.* **2014,** 105, 042105- 042110.
(35) Walsh, A.; Watson, G. W.; Payne, D. J.; Atkinson, G.; Egdell, R. G., A theoretical and experimental study of the distorted pyrochlore $Bi_2Sn_2O_7$. *J. Mater. Chem.* **2006,** 16, 3452-3458. DOI: 10.1039/B606413B
(36) Walsh, A.; Payne, D. J.; Egdell, R. G.; Watson, G. W., Stereochemistry of post-transition metal oxides: revision of the classical lone pair model. *Chem. Soc. Rev.* **2011,** 40, 4455-4463.
(37) Wang, Z. L.; Bentley, J.; Evans, N. D., Valence state mapping of cobalt and manganese using near-edge fine structures. *Micron* **2000,** 31, 355-362.
(38) Wiendlocha, B.; Kutorasinski, K.; Kaprzyk, S.; Tobola, J., Recent progress in calculations of electronic and transport properties of disordered thermoelectric materials. *Scr. Mater.* **2016,** 111, 33-38.
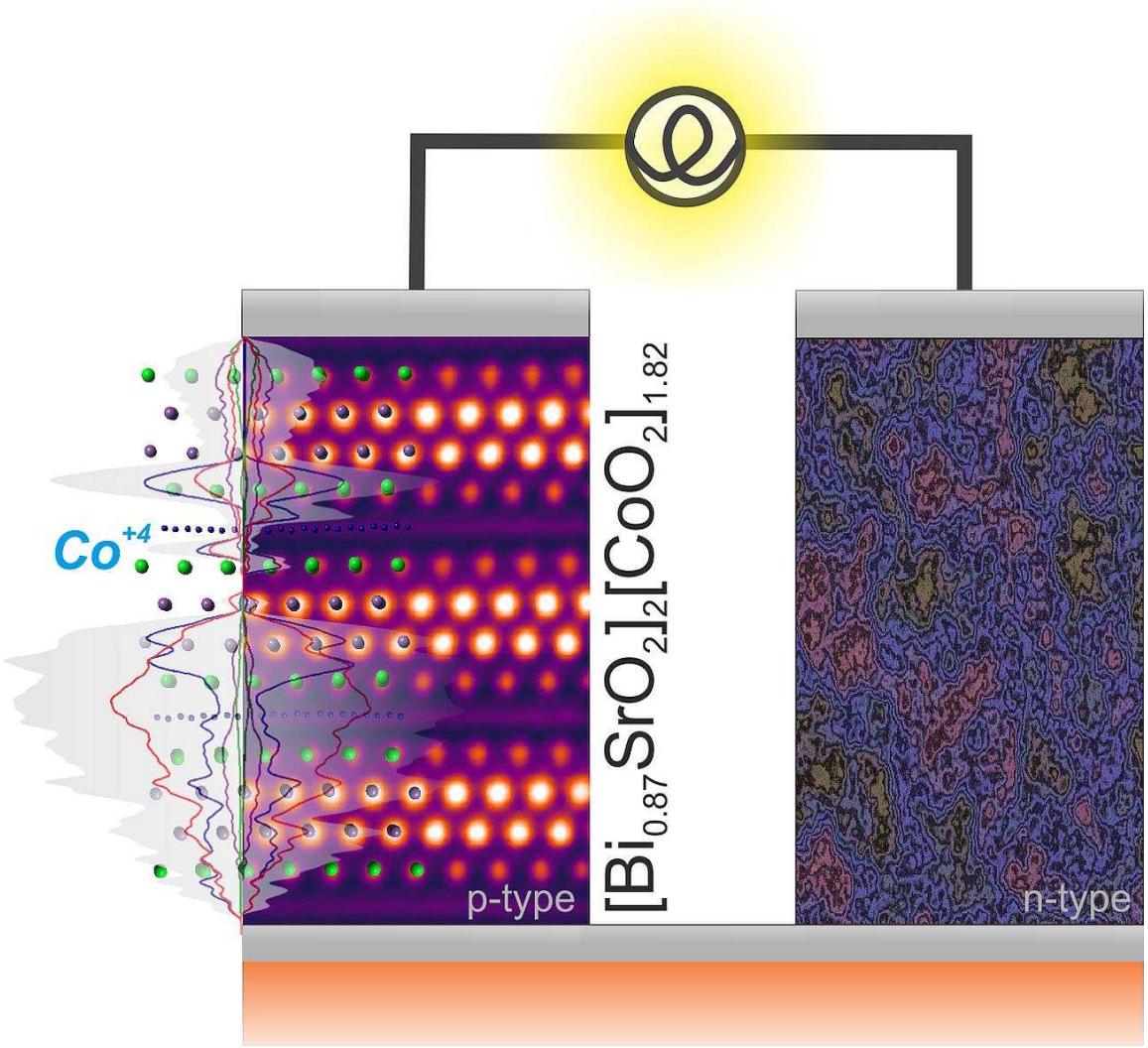
TOC